Fuel 236 (2019) 1065–1077

Contents lists available at ScienceDirect

Fuel

journal homepage: www.elsevier.com/locate/fuel

Full Length Article

Scaling law for slip flow of gases in nanoporous media from nanofluidics, rocks, and pore-scale simulations

Ye Tian[a], Xiangyu Yu[a], Jun Li[b], Keith B. Neeves[a], Xiaolong Yin[a], Yu-Shu Wu[a,*]

[a] Colorado School of Mines, Golden, CO 80401, USA
[b] Center for Integrative Petroleum Research, College of Petroleum Engineering and Geosciences, King Fahd University of Petroleum and Minerals, Saudi Arabia

ARTICLE INFO

Keywords:
Unconventional gas
Slip flow
Nanofluidics
Nanopores
DSBGK

ABSTRACT

In unconventional reservoirs, as the effective pore size becomes close to the mean free path of gas molecules, gas transport in porous media begins to deviate from Darcy's law. The objective of this study is to explore the similarities of gas flows in nanochannels and core samples as well as those simulated by direct simulation BGK (DSBGK), a particle-based method that solves the Bhatnagar-Gross-Krook (BGK) equation.

Due to difficulties in fabrication and experimentation, previous study on gas flow experiments in nanochannels is very limited. In this work, steady-state gas flow was measured in reactive-ion etched nanochannels with a controlled channel size on a sillicon wafer. A core-based permeability measurement apparatus was used to perform steady-state gas flow measurements on carbonate and shale samples. Klinkenberg permeability was obtained under varying pore pressures but constant temperature and effective stress. Methane was used in nanofluidic and rock experiments, making them directly comparable. Results from both experiments were then compared to gas flow simulations by DSBGK method carried out on several independently constructed geometry models. DSBGK uses hundreds of millions of simulated molecules to approximate gas flow inside the pore space. The intermolecular collisions are handled by directly integrating the BGK equation along each molecules trajectory, rather than through a sampling scheme like that in the direct simulation Monte-Carlo (DSMC) method. Consequently, the stochastic noise is significantly reduced, and simulation of nano-scale gas flows in complex geometries becomes computationally affordable.

The slippage factors obtained from these independent studies varied across three orders of magnitude, yet they all appear to collapse on a single scaling relation where the slippage factor in the slip flow regime is inversely proportional to the square root of intrinsic permeability over porosity. Our correlation could also fit the data in the literature, which were often obtained using nitrogen, after correcting for temperature and gas properties. This study contributes to rock characterization, well testing analysis as well as the understanding of rarefied gas transport in porous media.

1. Introduction

Even with the significant progress made in producing oil and gas from unconventional reservoirs with multistage fractured horizontal wells in the past decades, the recovery factor of hydrocarbons from these reservoirs remains very low. For gas reservoirs, the estimated recovery factor varies in the range of 5–30% while for oil reservoirs it is often <10% [1]. Compared with conventional reservoirs, the significant amount of residual hydrocarbons and substantial initial investments in drilling and stimulation make it pressing to develop practical tools to improve recovery factors and maximize the net present value. Gas slippage in the matrix has a significant impact on production performance of unconventional gas wells as well as modeling of unconventional gas reservoirs [2,3]. Moreover, it could also affect unconventional oil reservoirs as gas injection has become the top choice for EOR pilot tests in unconventional reservoirs [4]. Hence understanding the physics of gas flow in nanoporous rocks becomes crucial.

1.1. Empirical correlations for Klinkenberg coefficient

In the tight matrix of unconventional reservoirs, Klinkenberg effect would govern gas transport when the mean free path of gas molecules approaches the pore size in the nanoscale. According to Klinkenberg (1941) [5], the apparent permeability of gas k_g increases with decreasing average pressure and apparent gas permeability is given as,

* Corresponding author.
E-mail address: ywu@mines.edu (Y.-S. Wu).

https://doi.org/10.1016/j.fuel.2018.09.036
Received 9 June 2018; Received in revised form 1 September 2018; Accepted 7 September 2018
Available online 24 September 2018
0016-2361/ Published by Elsevier Ltd.

Table 1
Klinkenberg coefficient b as a power-law function of k_∞.

References	α	β	Gas
Heid et al. 1950 [6]	0.1106	−0.39	Air
Jones, 1972 [7]	0.1885	−0.36	N_2
Jones and Owens, 1980 [8]	0.9735	−0.33	N_2
Tanikawa and Shimamoto, 2009 [9]	0.1500	−0.37	N_2

$$k_g = k_\infty\left(1 + \frac{b}{\overline{p}}\right) \tag{1}$$

where b is the Klinkenberg coefficient (or slippage factor). In reservoir simulators, Klinkenberg effect can be modelled with different choices of Klinkenberg coefficient b. Characterization of Klinkenberg coefficient is hence of great value. Klinkenberg (1941) [5] proposed to relate b to the ratio between the mean free path λ and the characteristic dimension (radius) of pores r,

$$b = \frac{4c\lambda\overline{p}}{r} \tag{2}$$

However, since r is usually not directly measured for rocks, b is often empirically expressed as a power-law function of the intrinsic permeability of rock k_∞ for practical reservoir engineering purpose, i.e., $b = \alpha k_\infty^\beta$ as shown in Table 1.

By assuming that flow through porous media can be modelled by a bundle of capillary tubes, some researchers proposed that b should be a power-law function of k_∞/ϕ, i.e., $b = \alpha(k_\infty/\phi)^\beta$ as shown in Table 2. Most correlations in Table 2 have β as −0.5, which comes from replacing r in Eq. (2) by $(k_\infty/\phi)^{-0.5}$.

However, most current studies of gas slippage in cores often lacks the characterization of porosity let alone pore sizes. The effects of changing temperature, effective stress, and gas species on the slippage factor b are seldom systematically measured on the same rock. In order to better understand the above effects, the physics that leads to Klinkenberg effect needs to be reviewed.

1.2. Theoretical slippage factors

It is recognized that Klinkenberg effect can be all or partly attributed to gas rarefaction that can further be classified into four categories based on the Knudsen number [13] which is defined as,

$$\mathrm{Kn} = \frac{\lambda}{L} \tag{3}$$

where λ is the mean free path of gas molecules and L is a characteristic length. When Kn $<10^{-3}$, effect of gas rarefaction can be neglected, and the flow can be accurately modeled by the compressible Naiver-Stokes (N-S) equations with classical no-slip boundary conditions. When $10^{-3} < \mathrm{Kn} < 10^{-1}$, the flow is in the slip flow regime and the N-S equations remain applicable, provided that a velocity slip is applied to the wall. The slip velocity can be correlated to the velocity gradient normal to the wall through, for instance, a first-order slip model [14]. When $10^{-1} < \mathrm{Kn} < 10$, the flow regime is termed transitional, and the continuum approach of the N-S equations is no longer valid. When Kn>10, the flow enters the free molecular flow regime and the occurrence of intermolecular collisions is negligible compared with the collisions between the gas molecules and the walls. DSMC is a powerful tool for flows in these two regimes. DSBGK as an alternate simulation method achieves higher efficiency with the same level of accuracy as DSMC [39]. DSBGK agrees very well with experimental data [40] and the DSMC method over a wide range of Kn [15], even if Kn$<10^{-1}$ due to high pressure, because its molecular reflection boundary condition and governing equation are generally valid for any Kn. In this work, the DSBGK method was applied to simulate flow in a wide range of Kn but only data within the Kn range of (0.01, 0.1) were selected to extract the intrinsic permeability and slippage factor b to study the scaling law for the slip flow regime.

Table 2
Klinkenberg coefficient b as a power-law function of k_∞/ϕ.

References	α	β	Gas
Sampath and Keighim, 1982 [10]	0.0011	−0.53	N_2
Florence et al. 2007 [11]	0.0094	−0.5	N_2
Florence et al. 2007 [11]	0.0096	−0.5	Air
Civan, 2010 [12]	0.0094	−0.5	N_2

The above classification of gas flow regimes based on Kn is qualitative as different choices of characteristic lengths would lead to different limits. For flow in microchannels, L is generally chosen to be the hydraulic diameter or the depth of the channel. In porous rocks, pore diameter should be used as the characteristic length. For complex geometries [16], it could be preferable to calculate L from local gradients (for example of the density ρ: $L = \rho/|\nabla\rho|$). Klinkenberg coefficients for slip flows through simple geometries, such as those between parallel plates or within capillary tubes, can be obtained by solving the N-S equation with the first-order slip boundary condition,

$$u_{\mathrm{slip}} = -\frac{2-\sigma}{\sigma}\lambda\left(\frac{\partial u}{\partial n}\right)_{\mathrm{wall}} \tag{4}$$

where σ is the tangential momentum accommodation coefficient (TMAC). For gas flows between two parallel plates [17],

$$\frac{k_g}{k_\infty} = 1 + \frac{6(2-\sigma)}{\sigma}\frac{\lambda}{h} \tag{5}$$

The characteristic length is the distance between the two plates, i.e., $L = h$, provided that h is much smaller than the size of the plate. The expression for b is therefore,

$$b = 6p\mathrm{Kn}\frac{2-\sigma}{\sigma} \tag{6}$$

Similarly, for flows within a cylindrical tube,

$$\frac{k_g}{k_\infty} = 1 + \frac{4(2-\sigma)}{\sigma}\frac{\lambda}{r} \tag{7}$$

By defining the characteristic length as the hydraulic diameter, i.e., $L = 2r$, the expression for b is therefore,

$$b = 8p\mathrm{Kn}\frac{2-\sigma}{\sigma} \tag{8}$$

The above expressions for b motivated a general correlation for the gas slippage factor,

$$b = k_1 p\mathrm{Kn}\frac{2-\sigma}{\sigma} \tag{9}$$

Here, k_1 is a factor based on the geometry, e.g., cross-section shape. Kn can be calculated once the mean free path is calculated using the gas kinetic theory. For classic collision models, based on an inverse-power-law (IPL) interaction scheme, the expression of mean free path can be written as [16],

$$\lambda = \frac{k_2\mu}{\rho}\sqrt{\frac{M_w}{RT}} \tag{10}$$

where M_w is molecular weight in kg/mol; R is the universal gas constant in J/(K·mol), and Z is the compressibility factor; and k_2 is a constant from the viscosity model and is directly related to viscosity index given by [18]. For real gases,

$$\lambda = \frac{k_2\mu Z}{p}\sqrt{\frac{RT}{M_w}} \tag{11}$$

The pore radius r is often scaled to the square root of permeability k over porosity ϕ as $r \sim \sqrt{k/\phi}$. Now a general expression for the slippage

factor can be written as,

$$b \sim k_1 k_2 \frac{\mu Z}{\sqrt{k\phi}} \sqrt{\frac{RT}{M_w}} \frac{2-\sigma}{\sigma} \tag{12}$$

For flows in the slip flow regime with the first order slip boundary condition, Eq. (12) can be used to correlate b with respect to fluid properties (k_2, μ, Z, M_w), rock properties (k_1, k, ϕ), an empirical parameter σ and temperature T.

In most gas flows in experimental studies, flow is within the slip flow regime (Kn<0.1) and b appears as a constant independent of testing pressure. This is because the flow pressure is often high compared with the threshold pressure below which Kn can exceed 0.1. Additional reasons for b to appear as a constant include: the flow is isothermal, the pore size change in the lab is limited due to limited effective stress change and steady-state flow condition, and the product μZ is mostly constant for most experiments where $p < 2000$ psia (1.38×10^7 Pa).

Eq. (12) is no longer valid when Kn >0.1, which might exist in experiments with very low pressure [21] or in very tight matrix rock under proper reservoir conditions [22]. One approach to model gas flow in this regime is to use a function to asymptotically approximate the velocity near the wall surface using the result from DSMC[19,20].

$$\tilde{u}_{\text{slip}} = f\left(\sigma, Kn, \tilde{u}, \frac{\partial \tilde{u}}{\partial \tilde{n}}\right) \tag{13}$$

Another approach is to introduce high order terms, e.g., a second order term [21,22] to model slip velocity on the wall,

$$\tilde{u}_{\text{slip}} = C_1 \text{Kn}\left(\frac{\partial \tilde{u}}{\partial \tilde{n}}\right)_{\text{wall}} + C_2 \text{Kn}^2\left(\frac{\partial^2 \tilde{u}}{\partial \tilde{n}^2}\right)_{\text{wall}} \tag{14}$$

In the above models, the dimensionless velocity and distance are defined as,

$$\tilde{u} = u/u_0 \quad \tilde{n} = n/L$$

where u_0 is a characteristic velocity, e.g., the average inlet velocity; and n is the distance from the point of interest to the wall surface. The above models can be used up to Kn = $O(1)$ except Beskok and Karniadakis (1999) [19], which might be applicable up to the free molecular limit. In addition to the above models that focus on the boundary condition at gas–solid surfaces, Ertekin et al. (1986) [23] derived a dynamic slippage factor by assuming that the additional mass flux is due to Knudsen diffusion.

$$b = \frac{p c_g D_g \mu}{k_\infty} \tag{15}$$

where c_g is gas compressibility and D_g is the effective gas diffusivity in porous media. The concept of equating the viscous slip term with the diffusive flux can be traced back to the formulation of the Dusty Gas Model (DGM). When applying DGM to model single phase gas transport in porous media, Mason et al. (1967) [24] suggested that the origin of the slip term is just a diffusive component in DGM formulation. Researchers used measured Klinkenberg coefficients to calculate Knudsen diffusivities as detailed in [25]. However, it should be noted that Knudsen diffusion only applies in the free molecular region where Kn>10. In the slip flow regime where Kn<0.1 viscous flow should still be the dominating mode of transport [26]. The idea behind Eq. (12) and Eq. (15) of equating the effect of wall slip to Knudsen diffusion to arrive at an equation for b is physically incorrect (as shown in the Appendix). However, the idea of treating Klinkenberg coefficient as a dynamic variable, if implemented correctly, is useful as it allows us to handle situations more accurately when (a) the reservoir is subject to significant pore size changes e.g., geomechanical effects; (b) the reservoir has a high pressure where μZ can no longer be treated as constant; (c) the reservoir is non-isothermal e.g., geothermal reservoirs; (d) the rock matrix is tight enough to make Kn greater than 0.1.

To summarize, though core-based experiments could generate correlations directly useful to reservoir models, to fully understand the effects of gas species, pressure, temperature, and pore size, a scaling relation for b like Eq. (12) is needed. In this work, we use Klinkenberg coefficients obtained from simulated rarefied gas flows in simple geometries with known pore sizes and from experiments of gas flows in rectangular nanofluidic channels to check the validity of Eq. (12). The results were then compared with core experiments. Our correlation established from these data was then compared with data in the literature. In this comparison, the effects of temperature and gas were considered to approach a unified correlation for the dynamic slippage factor.

2. Methodology

2.1. Set-up of core experiments

Permeability measurements on low permeability rocks have been studied by many researchers [27–34]. Investigations above have shown that gas slippage factors measured in cores could be affected by geomechanical effects, temperature and gas species. Additionally, the measurement accuracy must be ensured by carefully designing the experimental setup and procedures. Rushing et al. (2014) [28] recommended steady-state measurements over unsteady-state due to the overestimation of results. Control in back pressure was recommended to remove inertial effects caused by high pressure gradient. Therefore, steady-state measurements were applied in this study, and back pressure was controlled to ensure a constant pressure gradient across the core for all pore pressures. The compaction effect by confining has been investigated by many studies [30,32–34] all of which concluded that effective stress could impact permeability, porosity and gas slippage. In this study, Biot's coefficient was assumed to be 1 and the confining pressure was loaded based on the average pore pressure to maintain a constant effective stress, aiming to remove the geomechanical effect on gas slippage. In addition, it was implied that temperature and gas species can all potentially impact apparent permeability and slippage [27,29,31]. Hence, temperature and was kept constant for flow tests.

As mentioned above, the experimental set-up, shown in Fig. 1, was assembled to conduct steady-state gas flow measurements in nanoporous rock samples at different pore pressures and confining stresses. Two gases were used for flow experiments: nitrogen and methane. Two types of rocks were used, i.e., Wisconsin carbonate (from Kocurek Industries) and Niobrara shale (from CEMEX Quarry, Colorado).

Before flow tests, core samples were cleaned and dried. Toluene was used for cleaning oil components and methanol was used for removing aqueous components. Soxhlet extractors were employed to clean cores for three weeks using toluene and two weeks using methanol, aiming to removing all fluids that resided in the rocks. After cleaning, the cores were dried in ovens. Cylindrical core samples have a diameter of 1.5 inches (3.81 cm) and a length of 2 inches (5.08 cm). A nitrogen gas tank was used to apply the confining pressure. An ISCO 260D pump was used to inject gas at a constant inlet pressure. A back-pressure regulator (FRT 6100, Chandler Engineering) was installed to maintain a constant outlet pressure. Inlet and outlet pressures were monitored by gauges (GE DPI-104) that were also connected to a computer for data logging.

Leakage tests were performed prior to flow tests. Pressurized gas was injected into the system and the readings of gauge 1 and gauge 2 were monitored during a test. Pressure loss rate was deemed acceptable when it was lower than 1 psia/hr (6.9×10^3 Pa/hr). This rate implies that leakage rate is less than 1% of typical gas flow rates. Each time when any part of the set-up was disassembled, the leakage test was repeated. Before flow tests, the rock core sample were pre-stressed with an effective stress 25% higher than the test effective stress for 48–72 h [32]. For example, if the desired average pore pressure is 300 psia (2.1×10^6 Pa) and the desired effective stress is 720 psia (5.0×10^6 Pa), the confining stress applied during pre-stressing will be 1,200 psia

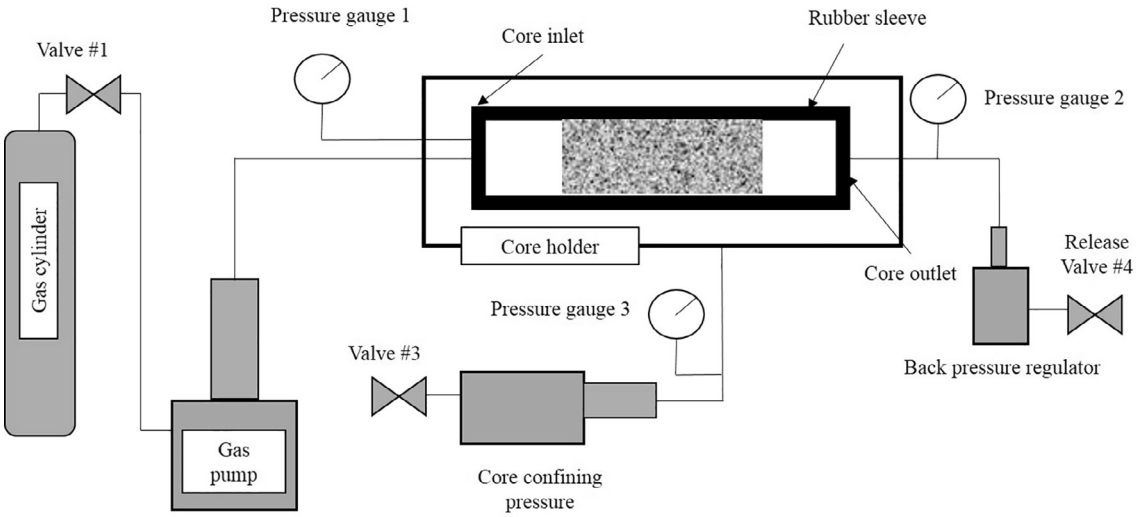

Fig. 1. The experimental set-up of gas flow measurement in cores.

(8.3×10^6 Pa) so that the effective stress is 900 psia (6.2×10^6 Pa), 25% higher than 720 psia (5.0×10^6 Pa). The set-up was initially benchmarked with brine flows through standard Berea cores. The measured absolute permeability was also benchmarked with a permeameter (Core Lab CMS300). The procedure of gas flow experiments is as follow:

1. Seal the core holder and apply confining pressure to maintain a constant effective stress as 720 psia (5.0×10^6 Pa) for all tests.
2. Pump gas into flow line and set back pressure higher than the desired pore pressure to close the outflow. Constant pressure injection mode was used to let the system reach desired pore pressure.
3. Stop injection and keep the system pressurized for 48–72 h to remove inelastic deformation. Meanwhile, the pressure was monitored to ensure the leakage for both flow line system and confining system were within acceptable levels.
4. Lower the back pressure to the desired outlet pressure and pump gas into the core until designed inlet pressure is reached. When reaching the steady state, both pressures should be stable and the variations of flow rate should diminish.
5. The pressure and pump volumetric data were logged into a computer for every 10 s. Flow rates were then computed by plotting pump chamber's volume with respect to time.

After reaching the steady state (after 10 h), each section of 20-min data was extracted and used for computing the flow rate, average inlet and outlet pressures, gas compressibility factor and viscosity. Gas compressibility factor Z was calculated by Peng-Robinson EOS. The flow rate was converted to that at the standard condition for calculating the apparent permeability. Viscosities of both gases were calculated by the correlation [35] and was also verified with NIST (National Institute of Standards and Technology) database (https://webbook.nist.gov/chemistry/). The viscosity and compressibility factor data were also applied to the analysis of nanofluidic experiments. The apparent permeability was obtained by:

$$k_g = \frac{q p_{\text{in}} \overline{Z} \overline{\mu} L}{Z_{\text{in}} \frac{\pi}{4} d^2 \frac{(p_{\text{in}}^2 - p_{\text{out}}^2)}{2}} \tag{16}$$

The average of all calculated permeability was presented as the apparent permeability for a specific pore pressure.

2.2. Experimental set-up of nanofluidics

Nanofluidic chips were fabricated with photolithography and reactive-ion etching in a class-100 cleanroom at the Center for Nanophase Materials Sciences of Oak Ridge National Laboratory. Both microchannels and nanochannels were etched on a double-sided polished silicon wafer 300 μm in thickness. The fabrication process was similar to that presented in Wu et al. (2014) [36]. First, an array of 20 nanochannels spaced 30 μm edge to edge was etched on the photo-resist covered silicon wafer by a Reactive Ion Etcher (Oxford Plasma System 100). Etching was divided into two stages. The first stage was carried out for half of the desired etching time. Then, the etching rate was calibrated based on the depth achieved during the first stage using a profilometer (Tencor Instrument P10). The etching time for the second stage was then adjusted accordingly. After etching, the residual photoresist was stripped away in hot bath at 343.15 K for 1 h and then the wafer was cleaned for 10 min with O_2-Ar plasma (PVA TePla ION 40 Gas Plasma System). Then, another layer of photoresist was placed and developed on the silicon wafer for defining the microchannels. Microchannels with a depth ranging from 8 to 10 μm were etched using only a single stage as it is not necessary to accurately control the depth of microchannels. The chip was then cleaned by O2-Ar plasma and characterized by profilometer and SEM (FEI Helios Nanolab 600i FIB).

The width of the pattern that contains nanochannels is 600 μm with 20 channels (13.5 μm channel width) and channel length is 400 μm as shown in Fig. 2. As mentioned above, the channel depth was achieved by reactive-ion etching but the depth within a channel was not strictly uniform ranging from 361.9 nm (498.0–136.1 nm) to 739.0 nm

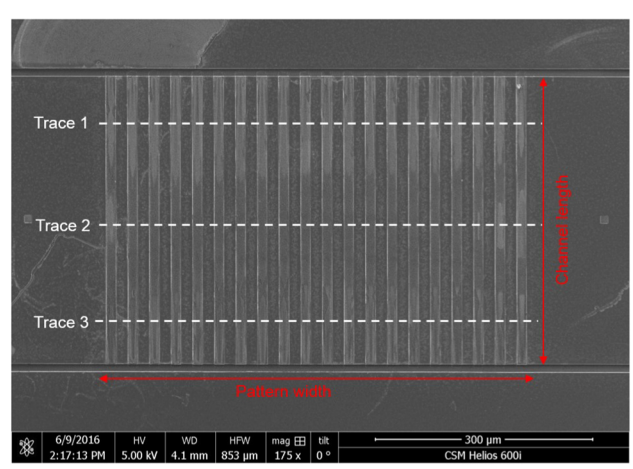

Fig. 2. Characterization of the nanochannel array with SEM.

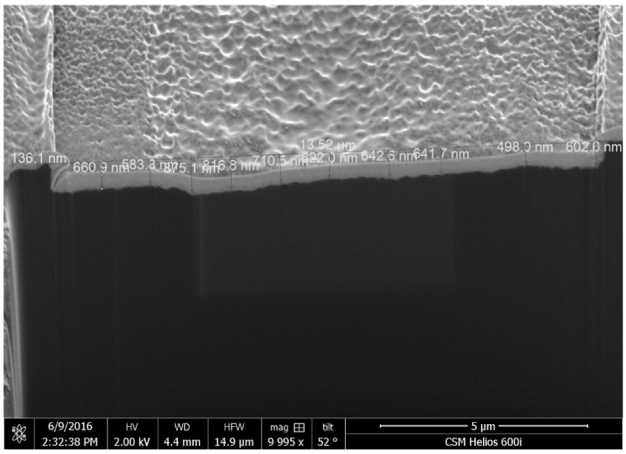

Fig. 3. Characterization of a single nanochannel with SEM.

(875.1–136.1 nm) as exemplified in Fig. 3 at the entrance of a nanochannel.

From the profilometer data shown in Figs. 4–6, the channel depth also varied based on locations (360 ± 53 nm for trace 1, 455 ± 31 nm for trace 2, and 456 ± 82 nm for trace 3) and from channel to channel. The approximate locations of traces are shown in Fig. 2. The channel-to-channel depth profile appears to be more uniform in the middle (Trace 2) than at the two ends. After the above characterizations, the front side of the wafer was bonded (573.15 K, 800 V, 15 min) to a thin Pyrex coverslip using a custom-built anodic bonder. The four holes on the backside of the wafer were connected to NanoPorts (IDEX) using liquid glue. Then, the nanofluidic device was ready to be connected to the flow system. The schematic of the lab-on-chip flow system is shown in Fig. 7. High-purity methane was injected to one port of the nanofluidic chip at a specific upstream pressure controlled by a pressure regulator. The downstream pressure was controlled by a back-pressure regulator. Four pressure gauges were used, of which two pressure gauges (p2, p3) were directly connected to the nanofluidic ports in order to better characterize the inlet and outlet pressure of the nanochannel arrays. When pressure is lower than 2000 psia (1.38×10^7 Pa), μZ can be treated as constant. We can therefore estimate the flow rate between the inlet and the outlet by using the squared form of pseudo pressure for inlet and outletwhich is more accurate for gases than the arithmetic mean used by Wu et al. (2014) [36].

$$p_{\text{in}} = \sqrt{\frac{p_1^2 + p_2^2}{2}} \quad p_{\text{out}} = \sqrt{\frac{p_3^2 + p_4^2}{2}}$$

The gas that left the nanofluidic chip through the back-pressure regulator was transported to and stored in a system composed of two tubes. The measuring tube was prefilled with dyed water and the vertical tube is used to prevent water backflow into the nanofluidics. As water was displaced by the accumulating methane, the volume change of methane was measured by recording the location of water meniscus in the measuring tube over a period. A typical flow measurement was done for three hours after a 12-h waiting period to assure that steady-state flow was reached. Once the flow rate was measured, the apparent permeability of the nanochannel array was calculated by,

$$k_g = \frac{\mu Z p_{\text{atm}}}{Z_{\text{atm}}} \frac{L_{\text{channel}}}{A_{\text{channel}}(p_{\text{in}}^2 - p_{\text{out}}^2)} \frac{\pi I D^2}{4} \frac{\Delta l}{\Delta t} \tag{17}$$

Before each run, a leakage test was conducted on the system, with all valves closed and the pressure of the nanochannel arrays monitored for three days. As the pressure variation due to leakage within a typical duration of a flow measurement e.g. three hours is 0.03 psia (207 Pa) which was much smaller compared with the full-scale accuracy of the pressure gauge (GE DPI 104) as 0.05 psia (345 Pa), leakage was deemed negligible.

2.3. Direct simulation method for BGK equation (DSBGK)

The BGK equation [37] can be solved to improve the computational efficiency in simulating gas flows at high Kn but at very low speeds [38,39]. The specific code used in this study was the DSBGK method developed in [39] and has been verified against the experimental study [40] as well as the DSMC method [18] as criterion in several benchmark problems over a wide range of Kn [15]. Although the DSBGK method is based on the BGK equation that uses a simple model to replace the intermolecular collision integral of the Boltzmann equation, it agrees very well with the DSMC method at high Kn. This is because the molecular reflection on the wall, the dominant effect in simulating

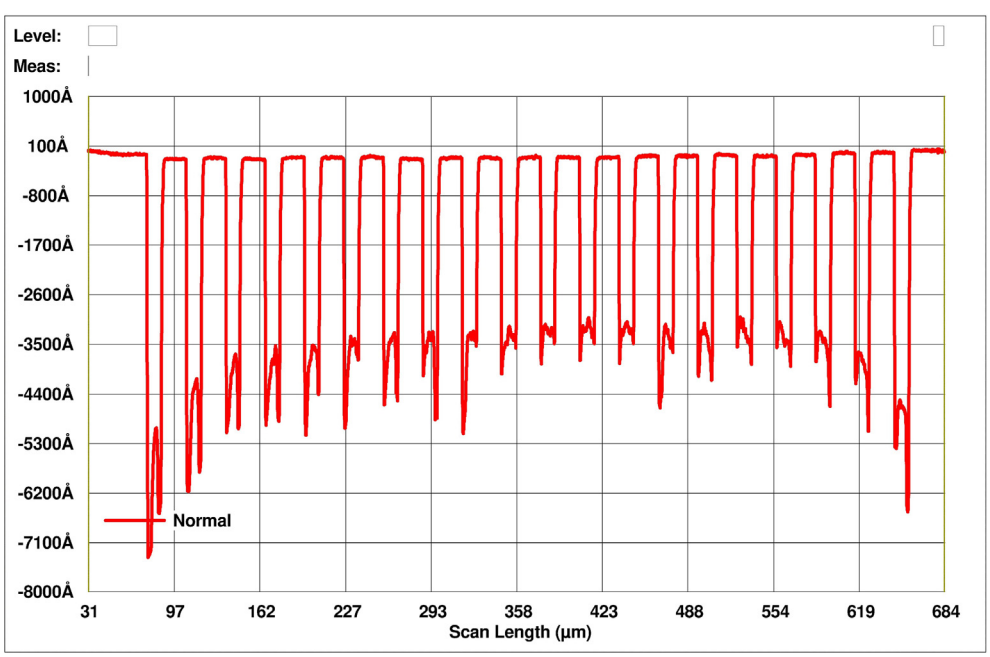

Fig. 4. The profile of channels measured along trace 1.

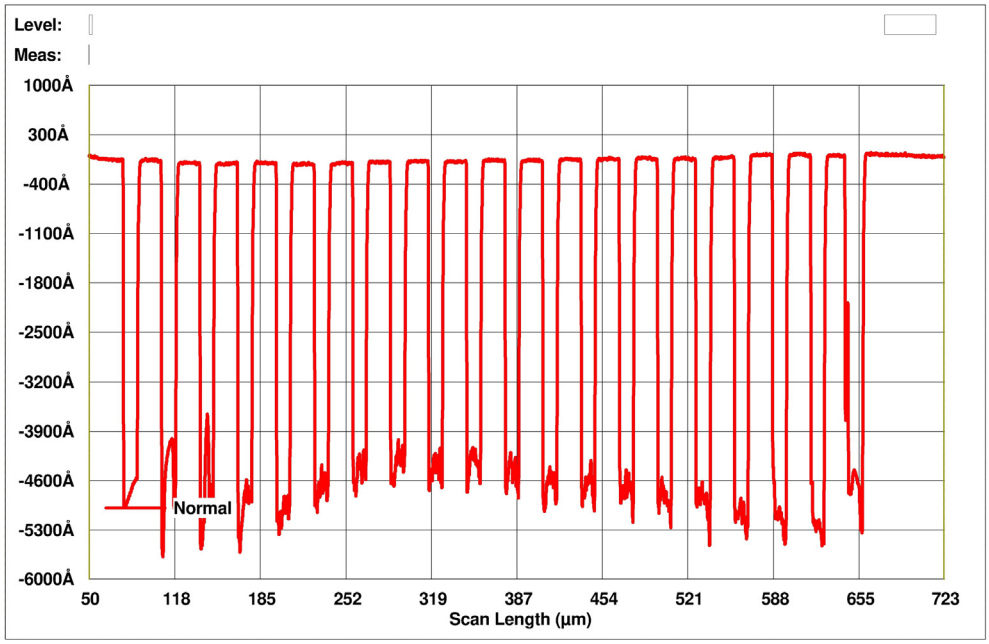

Fig. 5. The profile of channels measured along trace 2.

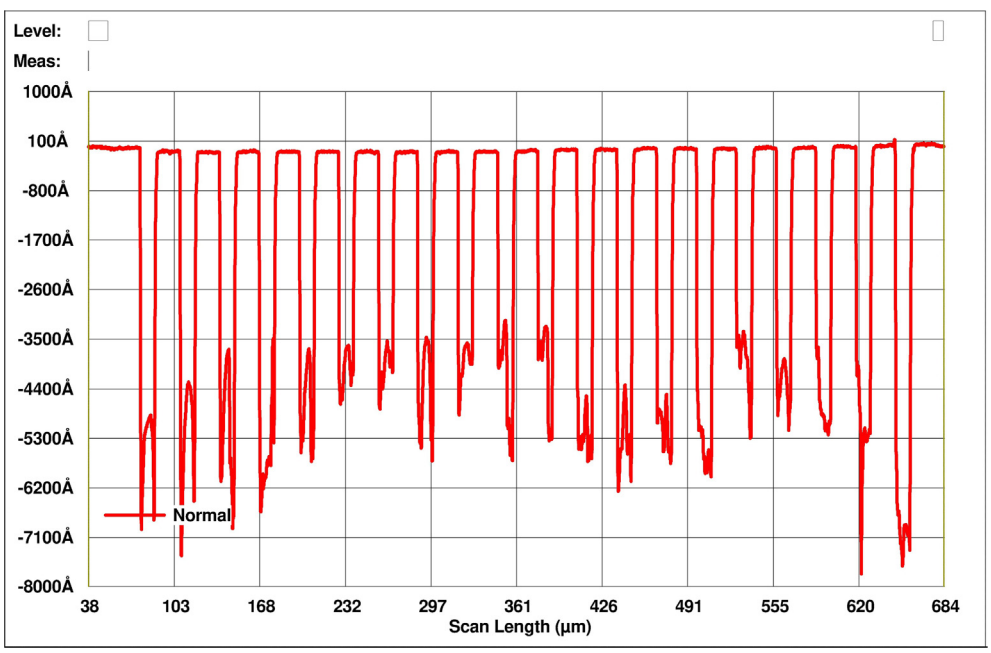

Fig. 6. The profile of channels measured along trace 3.

micro gas flows by kinetic methods, is modeled in the DSBGK method the same as in the DSMC method. Theoretically, the error due to this simplification disappears and the solution depends only on the boundary condition of molecular reflection when Kn approaches ∞. Compared with the standard DSMC method, the DSBGK method achieves high efficiency by avoiding generating a huge number of random fractions in the intermolecular collision process and using the increments (instead of transient values) of molecular variables to update cells macro quantities based on the conservation laws of mass, momentum and energy, which significantly reduces the stochastic noise due to discontinuous events of simulated molecules randomly moving into and out of cells. Theoretical analyses on algorithms of DSMC and DSBGK methods and the comparisons of simulation results between the two molecular simulation methods were detailed by Li (2012) [15]. Recently, it has been successfully applied to study the apparent permeability variation with pore pressure of gas flows in real shale samples by using the Fortran MPI software NanoGasSim [41].

A representative 2D nano-scale geometry as illustrated in Fig. 8 was used to study the variation in the apparent permeability with pore pressure. This geometry is characterized by dimensions W, S and L that can be adjusted to cover a wide range of porosity ϕ, intrinsic permeability k_∞ and pore body-to-throat ratios. In this study, five cases were considered and the parameter L was 100 nm for case 1 and fixed as 500 nm for other four cases, and combinations of W and S were used as follows: case 1 with $W = 10$ nm, $S = 20$ nm and $\phi = 0.22$; case 2 with $W = 10$ nm, $S = 90$ nm and $\phi = 0.094$; case 3 with $W = 10$ nm, $S = 10$ nm and $\phi = 0.0396$; case 4 with $W = 10$ nm, $S = 50$ nm and $\phi = 0.054$; case 5 with $W = 20$ nm, $S = 20$ nm and $\phi = 0.0784$. The

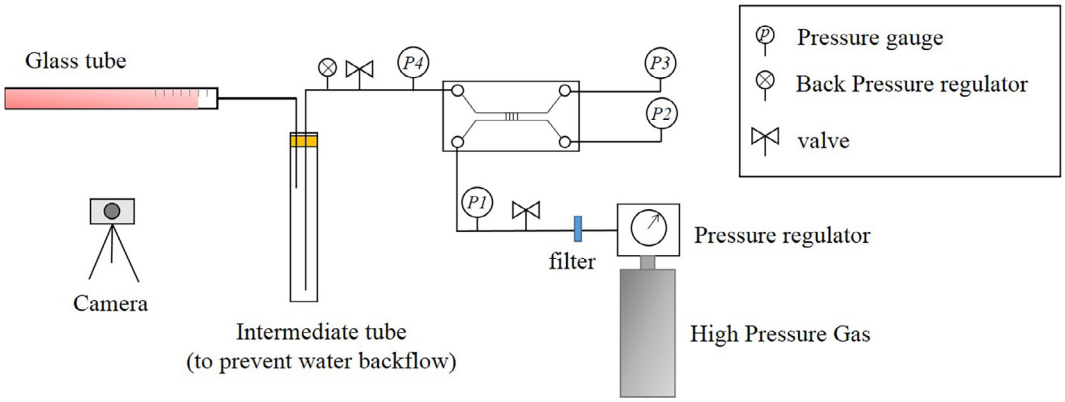

Fig. 7. The experimental set-up for measuring gas flow in nanofluidics.

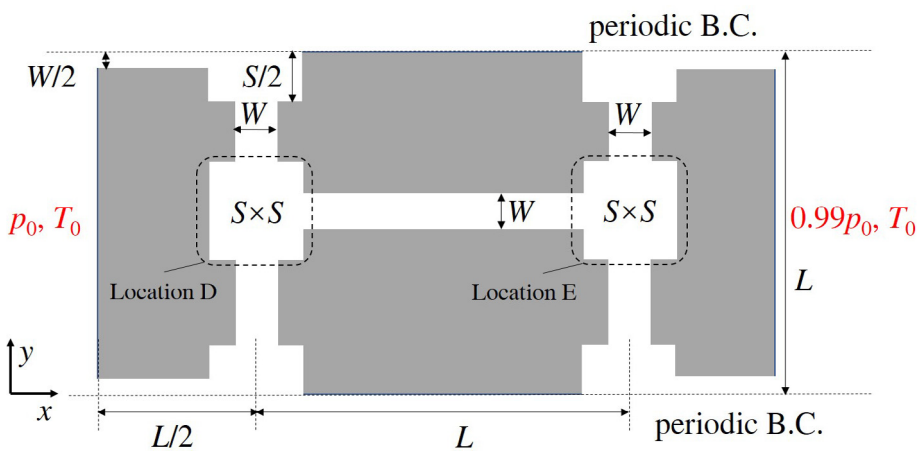

Fig. 8. The 2D geometry to study pressure-driven gas flows using DSBGK.

porosity is evaluated by the ratio of void area to the total area of the domain,

$$\phi = \frac{(2L-3S)W + 2S^2}{L^2} \tag{18}$$

Since simulated flows a isothermal, momentum exchange between colliding molecules is the dominant mechanism of relaxation. The relaxation coefficient υ of the BGK equation was therefore determined point-wise by the dynamic viscosity μ as follows,

$$\upsilon = \frac{n_d k_B T}{\mu} \tag{19}$$

where n_d is the local transient number density, k_B is the Boltzmann constant and T is the local transient temperature. The boundary condition used pure Maxwell diffuse reflection ($\sigma = 1$), which is accurate for molecular reflection processes at low speeds. Bird (1994) [18] summarized that experiments with most surfaces in contact with gases at normal temperatures have σ as 1. σ will only be much smaller than 1 for high-speed flows with shock waves on usual surfaces (not polished), or for flows over aircraft surfaces polished to reduce heat flux. In this work, we focused on flows within nanofluidics and nanoporous rocks, where σ as 1 should be a reasonable assumption for those rough surfaces. The initial temperature T_0 and the wall temperature T_{wall}, were set to 300 K. Methane were used in the simulations, and its viscosity is from the NIST database and assumed to be constant at a specified inlet pressure point because temperature variation is negligible due to the low Mach number of the flow and the pressure difference between inlet and outlet within the 2D domain is only 1% of inlet pressure. The effect of gas compressibility is negligible due to the small pressure difference, although the flows are modeled as compressible ($Z = 1$) in the DSBGK simulations.

As explained above, a BGK relaxation parameter is used to describe the effect of dynamic viscosity in DSBGK. There is no actual collision and viscosity could be an arbitrary function of temperature and density as observed in reality or from standard data provided by the NIST database. However, in order to set the flow condition within the first order slip flow regime, we need to maintain Kn within (0.01, 0.1). To calculate Kn, estimation of the mean free path was achieved by the hard sphere model (HS), which was consistently used in both simulations and experiments, i.e.,

$$\lambda_0 = \frac{16\mu}{5n_{d0}\sqrt{2\pi m k_B T_0}} \tag{20}$$

where m is the mass of one molecule in kg. For each geometry, the initial pore pressure related to the number density by $p_0 = n_{d0} k_B T_0$ was changed for the same geometry to cover a wide range of $\mathrm{Kn} = \lambda_0/W$. The pressure difference between the two ends was very small and hence steady-state apparent permeability k_g for each pressure point is evaluated according to the definition of permeability,

$$k_g = \frac{\mu\bar{u}}{\Delta p/2L} \tag{21}$$

where $\bar{u}$ is the average superficial velocity in m/s. Δp is the differential pressure between the inlet and outlet and $2L$ is the length of the 2D domain. About 10 simulations were used to obtain the apparent permeability variation with different p_0, from which the slope b of Klinkenberg law was extracted from the data located inside the slip flow regime where Kn<0.1. Similar to the standard of DSMC, time step Δt was selected to make the average moving distance per time step smaller than λ_0 and the cell size $\Delta x = \Delta y$ was smaller than λ_0 as well.

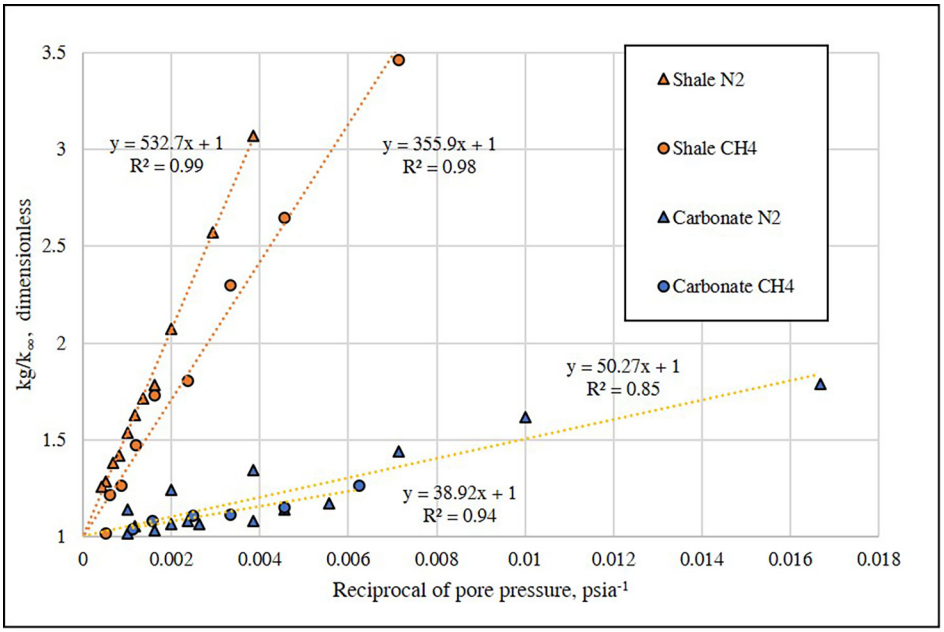

Fig. 9. Results from gas flow experiments through cores.

6000 × 3000 uniform cells were used at high pressure $p_0 = 25.77$ MPa with Kn as 0.02 and W as 10 nm. Additionally, at least eight cells were used to discretize the channel throat W at low pressure condition, where Δx is much smaller than λ_0, e.g., $\Delta x = 1.25$ nm and $\lambda_0 = 250$ nm at $p_0 = 20.6$ kPa with Kn as 25 and W as 10 nm. Each cell contains about 60 simulated molecules.

3. Results and discussions

3.1. Results of core experiments

Core flooding experiments generated four sets of results with two gases in two rock samples. Different pore pressures were applied for each set of experiments, ranging from 100 psia (6.89×10^5 Pa) to 2000 psia (1.38×10^7 Pa). Measured apparent permeability was normalized by the intrinsic permeability and plotted with its according reciprocal of the average pore pressure in Fig. 9. Measured slippage factors b with intrinsic permeability k_∞ are shown in Table 3. The slippage factors for both gases measured by Niobrara shale are larger than Wisconsin carbonate, which implies that Niobrara shale core might have a smaller average pore size than Wisconsin Carbonate core used in this study. The slippage factors estimated from methane flows for both cores are larger compared with those estimated by nitrogen flows.

3.2. Results of nanofluidic experiment

By assuming the flow rate was the same for each channel, the apparent permeability for a single channel can be calculated via Eq. (17). This apparent permeability is then plotted against the reciprocal of the average pressure as shown in Fig. 10. The intrinsic permeability for a single channel is 14.33 mD (1.41×10^{-14} m^2) and Klingenberg coefficient is 7.99 psia (5.51×10^4 Pa) by fitting the data to the Klinkenberg law,

$$k_g = k_\infty + \frac{bk_\infty}{(p_{in} + p_{out})/2} \tag{22}$$

On the other hand, the absolute permeability of a single channel with a rectangular cross-section can be calculated using the following expression [17].

$$k_\infty = \frac{h^2}{12} - \sum_{n=1}^{\infty} \frac{16h^3}{(2n+1)^5\pi^5 w} \tanh\left[\frac{(2n+1)\pi w}{2h}\right] \tag{23}$$

where h is the depth of a single nanochannel and w is the width of a single nanochannel. With intrinsic permeability as 14.33 mD, the average channel depth can be obtained as 416.1 nm from Eq. (23), which is comparable to the average depth measured by the profilometer.

Table 3
Summary of results from gas flow experiments through cores.

Core	Gas	k_∞, mD	k_∞, m^2	b, psia	b, Pa
Niobrara Shale	CH_4	1.24×10^{-4}	1.22×10^{-19}	355.9	2.45×10^6
	N_2	1.52×10^{-4}	1.50×10^{-19}	532.7	3.67×10^6
Wisconsin Carbonate	CH_4	1.76×10^{-2}	1.74×10^{-17}	38.92	2.68×10^5
	N_2	1.63×10^{-2}	1.61×10^{-17}	50.27	3.47×10^5

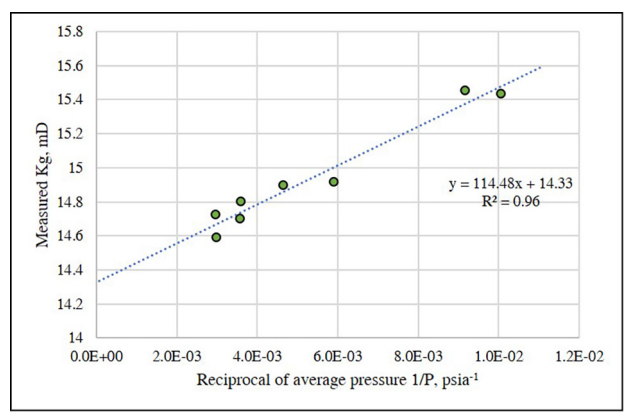

Fig. 10. Results from nanofluidic experiments.

3.3. Results of DSBGK

At very high pressures used in our study to cover the slip flow regime, Kn is low and the results of DSBGK should approach the solutions of the Navier–Stokes equation. We compared velocity fields at location

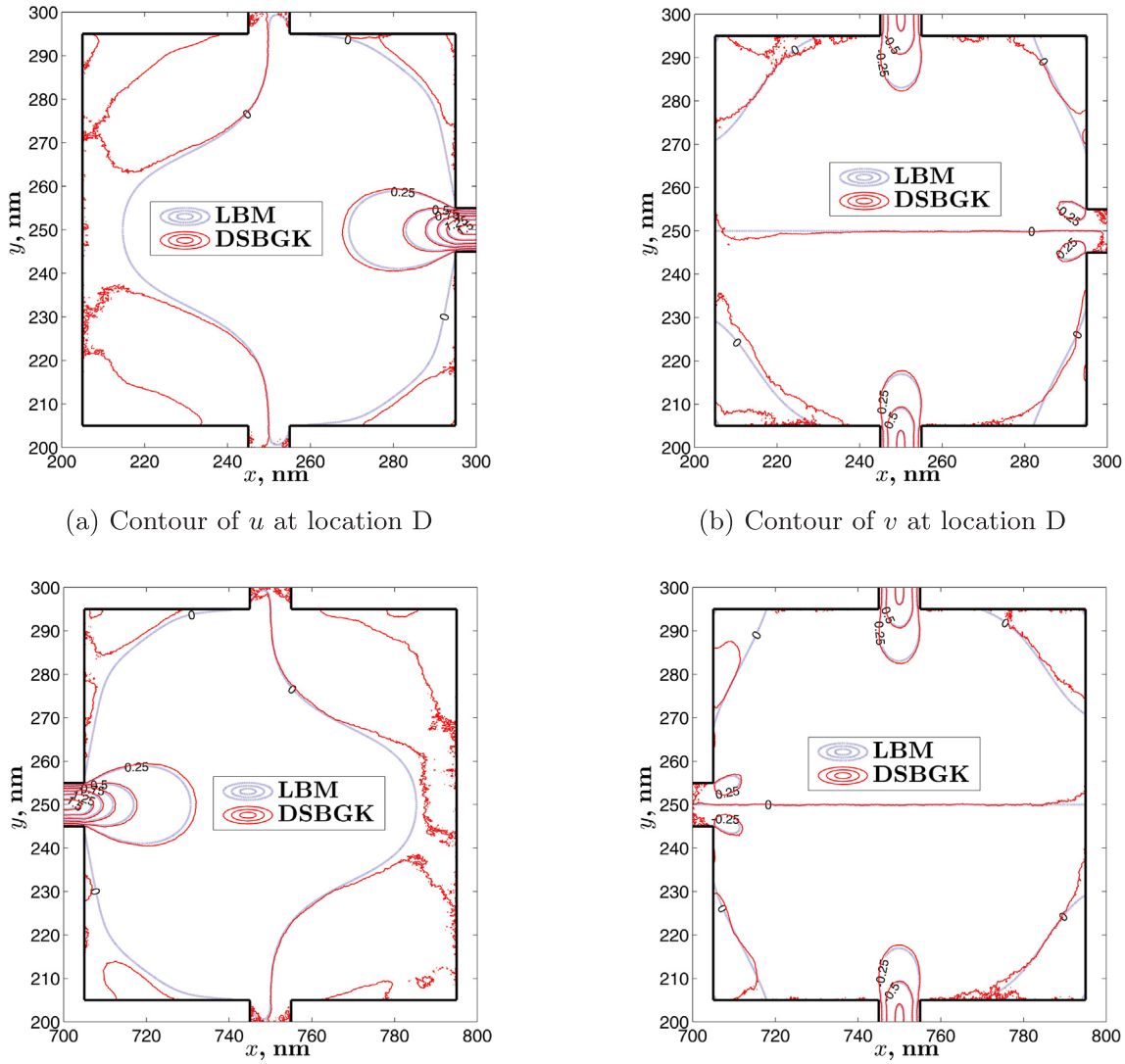

(a) Contour of u at location D

(b) Contour of v at location D

(c) Contour of u at location E

(d) Contour of v at location E

Fig. 11. Comparison of velocity contours between DSBGK and LBM (Case 1).

D and E of Fig. 8 from the DSBGK method at the highest pressure condition of $p_0 = 25.77$ MPa (Kn = 0.02) with those from an ordinary 2D Lattice Boltzmann Method (LBM) [42]. As shown in Fig. 11, the agreements of the DSBGK results of u and v velocity components at different locations with the LBM results are very good at this high pressure, which could be seen as a validation of DSBGK approach. Near channel exits and entrances, it is noticed that the velocity from DSBGK is slightly but consistently higher than that from LBM, showing the effect of slip. Since the standard Boltzmann equation is deemed invalid at high pressures due to violation of its two assumptions, i.e., molecular chaos and the dominance of binary inter-molecular collisions over ternary collisions, the BGK equation, which has removed these two assumptions, is a better approach for this study.

The intrinsic permeability and corresponding slippage factor for each case are summarized in Table 4. The simulated permeability normalized with intrinsic permeability is plotted against the reciprocal of the average pressure as shown in Fig. 12. The slippage factor b was extracted by a linear fitting of the computed apparent permeabilities in the first order slip regime with 0.01< Kn <0.1 and the intrinsic permeability was obtained by extrapolation to Kn = 0. The simulation results show that the intrinsic permeability depends mostly on the dominant pore throat size W, while the slippage factor b also noticeably depends on the porosity.

Table 4
Summary of DSBGK results.

Case	Gas	k_∞, mD	k_∞, m^2	b, psia	b, Pa
Case 1	CH_4	7.59×10^{-4}	7.49×10^{-19}	488.8	3.37×10^6
Case 2	CH_4	1.47×10^{-4}	1.45×10^{-19}	748.3	5.16×10^6
Case 3	CH_4	1.23×10^{-4}	1.21×10^{-19}	617.1	4.25×10^6
Case 4	CH_4	1.35×10^{-4}	1.33×10^{-19}	621.5	4.29×10^6
Case 5	CH_4	1.05×10^{-3}	1.04×10^{-18}	261.9	1.81×10^6

3.4. Comparison across core experiments, nanofluidic experiments, and DSBGK simulations

In Fig. 13, the slippage factors for methane obtained from these independent studies (nanofluidic experiments, core experiments, and DSBGK) are plotted as a function of k_∞/ϕ, following the scaling relation presented in Eq. (12). These data varied across three orders of magnitude yet they all appear to collapse on a single scaling relation,

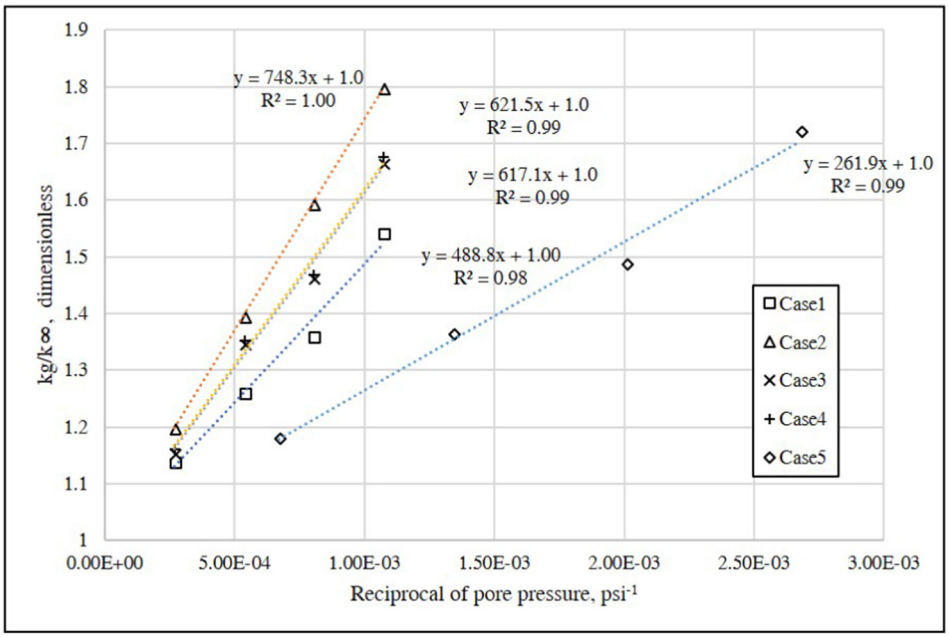

Fig. 12. Simulation results from DSBGK.

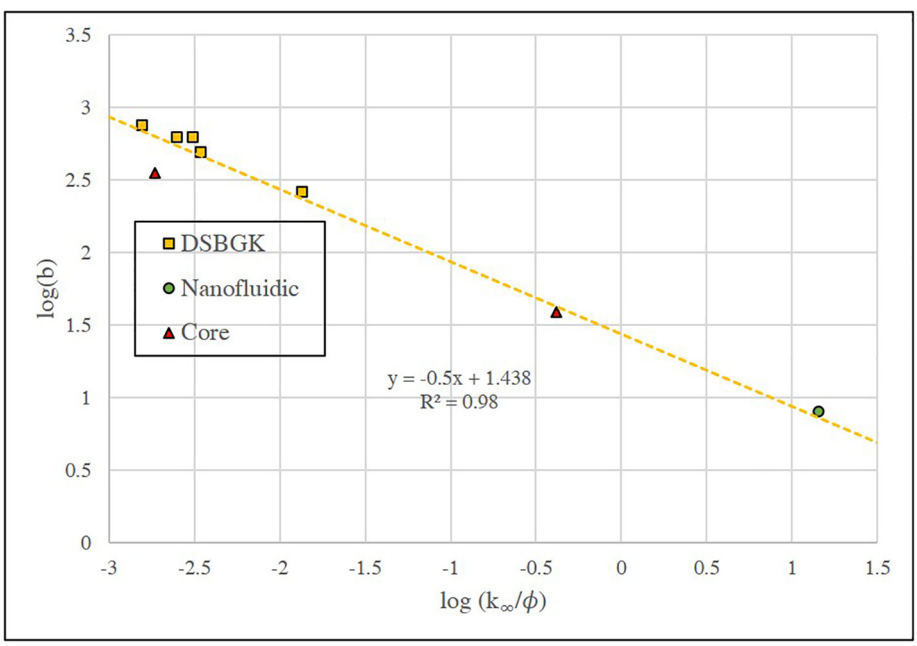

Fig. 13. Summary of slippage factors of methane obtained by different methods.

$$b = 10^{1.438}\left(\frac{k_\infty}{\phi}\right)^{-0.5} \tag{24}$$

where slippage factor b is in psia and intrinsic permeability k_∞ is in mD. The trend demonstrated in Fig. 13 indicates that the slippage factor in the slip flow regime is inversely proportional to the square root of intrinsic permeability over porosity as predicted by Eq. (12). Such a scaling relation has been proposed by previous researchers [11,12] as,

$$b = \beta\left(\frac{k_\infty}{\phi}\right)^{-0.5} \tag{25}$$

Civan (2010) [12] specifically proposed that,

$$\beta = \mu\sqrt{\frac{\pi RT}{\tau M_w}} \tag{26}$$

where τ is the rock tortuosity. Based on Civan (2010) [12], β can be calculated as 7.87×10^{-3} in SI unit by assuming tortuosity τ as 1. But, β directly calculated by using the intercept as 1.438 in our correlation is 5.94×10^{-3} after the unit conversion to SI. The difference may come from the fact that tortuosity τ mostly is larger than 1, and hence using τ as 1 may overestimate the slippage factor.

In Fig. 14, our correlation is compared to the gas slip flow data in the literature. Though there are many data in the literature regarding gas slip flows, we only selected the experimental data that come with known porosity, temperature and gas species. Qualified data from the literature hence becomes limited [10,11,43,44] and most of them are based on nitrogen and should be corrected for differences in temperature and gas species. This correction was achieved by re-scaling b with the condition of methane experiments. Note that the results of our own nitrogen experiments, included in Fig. 14, were corrected in the same

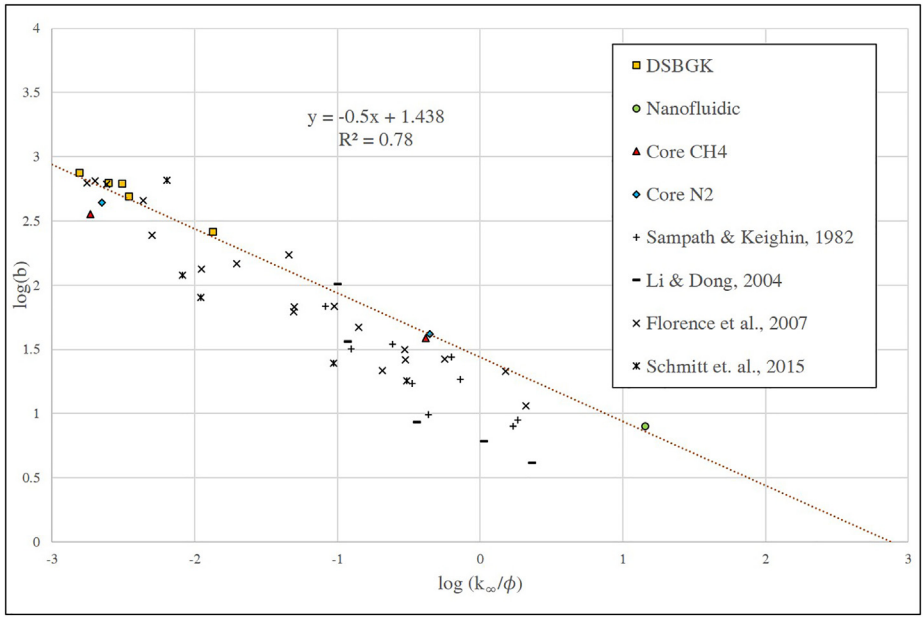

Fig. 14. *b* from litertature (converted to methane at 300 K) compared to this study.

way. For the same core at the same temperature, nitrogen tends to have larger *b* than methane. For Wisconsin carbonate, after scaling N_2's data with respect to viscosities, compressibility factors, and molecular weights, the scaled slippage factor of N_2 (41.5 psia) becomes very close to the slippage factor based on CH_4 (38.9 psia) as shown in Table 1. For Niobrara shale, the difference between scaled N_2's *b* (355.9 psia) and CH_4's *b* (439.8 psia) is still appreciable possibly due to the difference in CH_4 and N_2's adsorption with shale surfaces, a factor that is not considered in the slip flow model.

Our correlation Eq. (24) can fit these additional slip flow data with $R^2 = 0.78$, which illustrates the relevance of our correlation to data in the literature. Though a better match could be achieved with a slope as −0.60 and hence a R^2 of 0.90, we chose to hold the slope as −0.5 because of the requirement of dimensional consistency and also because most literature would scale the pore size with respect to permeability and porosity as $r \sim \sqrt{k/\phi}$. Eq. (24) based on methane at 300 K would also justify our choice of the slope. Slippage factors at other temperatures or for other gases can be obtained by scaling Eq. (24) with temperature and gas properties following Eq. (12), which approaches the concept of dynamic slippage factor in a practical way.

4. Conclusions

In most laboratory studies, isothermal flow within the slip flow regime (Kn <0.1) leads to a constant slippage factor. However, varying temperature or gas type will change the slippage factor. When a reservoir is subject to significant pore size changes due to geomechanical effects or the reservoir has a high pressure where μZ of gas can no longer be treated as constant, the slippage factor will also be discovered as a dynamic variable. The above effects are best described by Eq. (12) based on the theory of rarefied gas flows in the slip flow regime.

In this work, Klinkenberg coefficients from nanofluidic experiments and those from 2D DSBGK simulations were combined to establish a correlation in the form of Eq. (12). As the dimensions of rectangular channels in nanofluidics and those of the 2D geometries are known, Kn can be clearly limited to the slip flow regime where Eq. (12) is expected to hold. Then, the results from core experiments were added to the correlation. The slippage factors obtained from these independent studies varied across three orders of magnitude, yet they all collapse on a single scaling relation that follows the format of Eq. (12). Specifically, the slippage factors are inversely proportional to the square root of the intrinsic permeability over porosity. Our correlation matched data from the literature after those data were scaled with respect to temperature and gas type.

Unlike existing correlations in the literature, our correlation is established based on methane, which is a major component in unconventional gas reservoirs and a promising injectant for gas injection IOR/EOR. The correlation can be applied to estimate Klinkenberg coefficients at different temperatures and for other gases, by scaling the coefficient with temperature and gas species. Therefore it can be implemented easily into a reservoir simulator. This study contributes to rock characterization, well testing analysis, reservoir simulation as well as the understanding of rarefied gas transport in nanoporous media.

Acknowledgments

The authors would like to thank Energi Simulation, Oak Ridge National Laboratory, and Halliburton for their support.

Appendix A. Counter example regarding dynamic slippage factor based on Knudsen diffusion

The slip flow term should not be treated as equivalent to the Knudsen diffusion term in the slip flow regime even though they give a similar dependence on temperature and gas properties. Unfortunately, such a mistake could be commonly found in many research papers related to this topic. In what follows, an example was provided to demonstrate the inequivalence of the slip flow and Knudsen diffusion. Following the Dusty Gas Model (DGM), the expression for molar flux of a single-component gas [24] in a capillary tube is,

$$\frac{\vec{J_k}}{D^e_{k,Kn}} = -\nabla X_k - \frac{X_k}{D^e_{k,Kn}} \frac{B}{\mu} \nabla p$$

where $X_k = p/RT$ is the molar density for the gas phase that can be calculated using an ideal-gas EOS. The molar flux is hence related to the pressure gradient by,

$$\vec{J_k} = -\left(D^e_{k,Kn} + \frac{Bp}{\mu}\right)\frac{\nabla p}{RT}$$

assuming isothermal condition. With the following expressions for B and the effective Knudsen diffusivity,

$$B = \frac{r^2}{8}, \quad D^e_{k,Kn} = \frac{2}{3}r\sqrt{\frac{8RT}{\pi M_w}}$$

The expression for the molar flux is now [45],

$$\vec{J_k} = -\left(\frac{2}{3}r\sqrt{\frac{8RT}{\pi M_w}} + \frac{p}{\mu}\frac{r^2}{8}\right)\frac{\nabla p}{RT}$$

In the slip flow regime, the molar flux can be obtained by subjecting N-S equation to the first-order slip boundary.

$$\vec{J_k} = -\frac{\partial p}{\partial z}\frac{p}{\mu}\frac{1}{RT}\left(\frac{2-\sigma}{\sigma}\lambda\frac{r}{2} + \frac{r^2}{8}\right)\nabla p$$

By assuming these two expressions as equivalent,

$$\frac{2}{3}r\sqrt{\frac{8RT}{\pi M_w}} + \frac{p}{\mu}\frac{r^2}{8} = \frac{p}{\mu}\frac{2-\sigma}{\sigma}\lambda\frac{r}{2} + \frac{p}{\mu}\frac{r^2}{8}$$

Substitute the expression for the mean free path,

$$\lambda = \frac{k_2\mu Z}{p}\sqrt{\frac{RT}{M_w}}$$

and let $Z = 1$ (ideal gas) and $\sigma = 1$, and the following is arrived,

$$\frac{2}{3}r\sqrt{\frac{8RT}{\pi M_w}} = k_2\sqrt{\frac{RT}{M_w}}\frac{r}{2}$$

Hence,

$$k_2 = \frac{8}{3}\sqrt{\frac{2}{\pi}} = 2.128$$

A similar result was derived by Rose (1948) [46] and it was shown that the mean free path is,

$$\lambda = \frac{2.13\mu}{p}\sqrt{\frac{RT}{M_w}}$$

and this expression was used by Ertekin et al. (1986) [23]. However, according to classic IPL collision models summarized in [16,18], under the standard condition, k_2 can never be larger than 1.277. For the Hard Sphere (HS) gas,

$$k_2 = \frac{16}{5\sqrt{2\pi}} = 1.277$$

For gases that obey the VHS (Variable Hard Sphere) model ($0.5 < \omega < 1.5$), it can be proved that,

$$k_2 = \frac{2(7-2\omega)(5-2\omega)}{15\sqrt{2\pi}} \leqslant \frac{16}{5\sqrt{2\pi}} = 1.277$$

Similarly, with VSS (Variable Soft Sphere) gas model ($1 < \alpha < 2$), it can be proved that,

$$k_2 = \frac{4\alpha(7-2\omega)(5-2\omega)}{5(\alpha+1)(\alpha+2)\sqrt{2\pi}} \leqslant \frac{96}{5(2\sqrt{2}+3)\sqrt{2\pi}} < \frac{16}{5\sqrt{2\pi}} = 1.277$$

k_2 evaluated by Knudsen's diffusion model is always greater than that from the classic IPL collision models. Therefore, the slip flow term should not be treated as equivalent to the Knudsen diffusion term in the slip flow regime even though they may give a similar dependence on temperature and gas properties. Beskok and Karniadakis (1999) [19] drew a similar conclusion that Knudsens model would overpredict the mass flow rate in the slip flow regime, after comparing Knudsen's model with NIST data and the solution of linearized Boltzmann equation. In summary, the slippage factor should not be derived by Knudsen's diffusion model in the slip flow regime as it will always lead to an overestimation of the slippage effect.

References

[1] Wang L, Tian Y, Yu X, Wang C, Yao B, Wang S, et al. Advances in improved/enhanced oil recovery technologies for tight and shale reservoirs. Fuel 2017;210:425–45. https://doi.org/10.1016/j.fuel.2017.08.095.

[2] Wu YS, Li J, Ding D, Wang C, Di Y. A generalized framework model for the simulation of gas production in unconventional gas reservoirs. SPE J 2014;19(05):845–57.

[3] Zeng J, Wang X, Guo J, Zeng F. Composite linear flow model for multi-fractured horizontal wells in heterogeneous shale reservoir. J Nat Gas Sci Eng 2017;38:527–48.

[4] Sheng JJ. Enhanced oil recovery in shale reservoirs by gas injection. Journal of Natural Gas Science and Engineering 2015;22:252–9.

[5] Klinkenberg L. The permeability of porous media to liquids and gases. Drilling and production practice American Petroleum Institute; 1941.

[6] Heid J, McMahon J, Nielsen R, Yuster S. Study of the permeability of rocks to homogeneous fluids. Drilling and production practice American Petroleum Institute; 1950.

[7] Jones SC. A rapid accurate unsteady-state klinkenberg permeameter. Soc Pet Eng J

1972;12(05):383–97.
[8] Jones FO, Owens W. A laboratory study of low-permeability gas sands. J Pet Technol 1980;32(09):1–631.
[9] Tanikawa W, Shimamoto T. Comparison of klinkenberg-corrected gas permeability and water permeability in sedimentary rocks. Int J Rock Mech Mining Sci 2009;46(2):229–38.
[10] Sampath K, Keighin CW. Factors affecting gas slippage in tight sandstones of cretaceous age in the uinta basin. J Pet Technol 1982;34(11):2–715.
[11] Florence FA, Rushing J, Newsham KE, Blasingame TA. Improved permeability prediction relations for low permeability sands. Rocky Mountain Oil & Gas Technology Symposium Society of Petroleum Engineers; 2007.
[12] Civan F. Effective correlation of apparent gas permeability in tight porous media. Transp Porous Media 2010;82(2):375–84.
[13] Colin S. Single-phase gas flow in microchannels. Heat Transfer Fluid Flow Minichannels Microchannels 2014:9–86.
[14] Wang L, Yin X. Apparent permeability of flow through periodic arrays of spheres with first-order slip. Powder Technology 2017;311:313–27.
[15] Li J. Comparison between the dsmc and dsbgk methods. arXiv preprint arXiv:12071040; 2012;.
[16] Colin S. Pressure-driven single-phase gas flows. Encyclopedia Microfluidics Nanofluidics 2015:2835–46.
[17] Wang L. Simulation of slip flow and phase change in nanopores. Colorado School of Mines; 2014. [Ph.D. thesis].
[18] Bird G. Molecular gas dynamics and the direct simulation monte carlo of gas flows. Clarendon, Oxford 1994;508:128.
[19] Beskok A, Karniadakis GE. Report: a model for flows in channels, pipes, and ducts at micro and nano scales. Microscale Thermophys Eng 1999;3(1):43–77.
[20] Xue H, Fan Q. A new analytic solution of the Navier-Stokes equations for microchannel flows. Microscale Thermophys Eng 2000;4(2):125–43.
[21] Colin S, Lalonde P, Caen R. Validation of a second-order slip flow model in rectangular microchannels. Heat Transfer Eng 2004;25(3):23–30.
[22] Wang S, Lukyanov AA, Wang L, Wu YS, Pomerantz A, Xu W, Kleinberg R. A non-empirical gas slippage model for low to moderate knudsen numbers. Phys Fluids 2017;29(1):012004.
[23] Ertekin T, King GA, Schwerer FC. Dynamic gas slippage: a unique dual-mechanism approach to the flow of gas in tight formations. SPE Form Eval 1986;1(01):43–52.
[24] Mason E, Malinauskas A, Evans Iii R. Flow and diffusion of gases in porous media. J Chem Phys 1967;46(8):3199–216.
[25] Thorstenson DC, Pollock DW. Gas transport in unsaturated zones: Multicomponent systems and the adequacy of Fick's laws. Water Resour Res 1989;25(3):477–507.
[26] Wu K, Chen Z, Li X. Real gas transport through nanopores of varying cross-section type and shape in shale gas reservoirs. Chem Eng J 2015;281:813–25.
[27] Wei K, Morrow N, Brower K. Effect of fluid, confining pressure, and temperature on absolute permeabilities of low-permeability sandstones. SPE Form Eval 1986;1(04):413–23.
[28] Rushing J, Newsham K, Lasswell P, Cox J, Blasingame T. Klinkenerg-corrected permeability measurements in tight gas sands: steady-state versus unsteady-state techniques. SPE annual technical conference and exhibition Society of Petroleum Engineers; 2004.
[29] Alnoaimi K, Kovscek A. Experimental and numerical analysis of gas transport in shale including the role of sorption. SPE Annual Technical Conference and Exhibition Society of Petroleum Engineers; 2013.
[30] Cho Y, Ozkan E, Apaydin OG. Pressure-dependent natural-fracture permeability in shale and its effect on shale-gas well production. SPE Reservoir Eval. Eng. 2013;16(02):216–28.
[31] Sinha S, Braun E, Determan M, Passey Q, Leonardi S, Boros J, et al. Steady-state permeability measurements on intact shale samples at reservoir conditions-effect of stress, temperature, pressure, and type of gas. SPE Middle East oil and gas show and conference Society of Petroleum Engineers; 2013.
[32] Heller R, Vermylen J, Zoback M. Experimental investigation of matrix permeability of gas shales. AAPG Bull 2014;98(5):975–95.
[33] Pan Z, Ma Y, Danesh NN, Connell LD, Sander R, Down DI, et al. Measurement of shale anisotropic permeability and its impact on shale gas production. SPE Asia Pacific Unconventional Resources Conference and Exhibition Society of Petroleum Engineers; 2015.
[34] Letham E, Bustin R. Klinkenberg gas slippage measurements as a means for shale pore structure characterization. Geofluids 2016;16(2):264–78.
[35] Ling K. Gas viscosity at high pressure and high temperature. Texas A & M University; 2012. [Ph.D. thesis].
[36] Wu Q, Bai B, Ma Y, Ok JT, Yin X, Neeves K. Optic imaging of two-phase-flow behavior in 1d nanoscale channels. Spe J 2014;19(05):793–802.
[37] Bhatnagar PL, Gross EP, Krook M. A model for collision processes in gases. i. small amplitude processes in charged and neutral one-component systems. Phys Rev 1954;94(3):511.
[38] Ramanathan S, Koch DL. An efficient direct simulation monte carlo method for low mach number noncontinuum gas flows based on the Bhatnagar-Gross-Krook model. Phys Fluids 2009;21(3):033103.
[39] Li J. Direct simulation method based on bgk equation. AIP Conference Proceedings, vol. 1333. AIP; 2011. p. 283–8.
[40] Li J, Cai C. Numerical study on thermal transpiration flows through a rectangular channel. arXiv preprint arXiv:170808105; 2017.
[41] Li J, Sultan AS. Permeability computations of shale gas by the pore-scale monte carlo molecular simulations. In: International Petroleum Technology Conference. International Petroleum Technology Conference; 2015.
[42] Newman MS, Yin X. Lattice boltzmann simulation of non-darcy flow in stochastically generated 2d porous media geometries. SPE J 2013;18(01):12–26.
[43] Li S, Dong M, Li Z. Measurement and revised interpretation of gas flow behavior in tight reservoir cores. J Pet Sci Eng 2009;65(1–2):81–8.
[44] Schmitt M, Fernandes CP, Wolf FG, da Cunha Neto JAB, Rahner CP, dos Santos VSS. Characterization of brazilian tight gas sandstones relating permeability and angstrom-to micron-scale pore structures. J Nat Gas Sci Eng 2015;27:785–807.
[45] Wang J, Chen L, Kang Q, Rahman SS. Apparent permeability prediction of organic shale with generalized lattice boltzmann model considering surface diffusion effect. Fuel 2016;181:478–90.
[46] Rose WD. Permeability and gas-slippage phenomena. Drilling and production practice American Petroleum Institute; 1948.